Enhanced catalytic performance of CoO_x-CeO_2 for synergetic degradation of toluene in multistage sliding plasma system through response surface methodology (RSM)

Nan Jiang[a,b,d,*], Yonghe Zhao[a,c], Cheng Qiu[a,c], Kefeng Shang[a,b], Na Lu[a,b], Jie Li[a,b], Yan Wu[a,b], Ying Zhang[e]

[a] Key Laboratory of Industrial Ecology and Environmental Engineering, Ministry of Education of the People's Republic of China, Dalian 116024, China
[b] Institute of Electrostatics and Special Power, School of Electrical Engineering, Dalian University of Technology, Dalian 116024, China
[c] School of Environmental Science & Technology, Dalian University of Technology, Dalian 116024, China
[d] State Key Laboratory of Electrical Insulation and Power Equipment, Xi'an Jiaotong University, Xi'an, 710049, China
[e] College of Information Science and Technology, Nanjing Forestry University, Nanjing 210037, China

ARTICLE INFO

ABSTRACT

Post plasma-assisted catalysis for toluene degradation using nanosecond pulsed multistage sliding dielectric barrier discharge (multi-SLDBD) plasma over a series of CoO_x-CeO_2 catalysts has been studied at atmospheric pressure and ambient temperature. Several characterization methods including BET, XRD, SEM, HRTEM, XPS, and H_2-TPR have been utilized to evaluate the influence of Co/Ce molar ratio on the catalyst physiochemical properties. When the multi-SLDBD plasma was combined with catalyst, an obvious improvement could be obtained in toluene degradation efficiency compared to plasma alone even at low *SIE*. The incorporation of Ce into Co oxides presented higher catalytic activity for toluene degradation and mineralization than Co oxide, which can be ascribed to higher content of surface-adsorbed oxygen (O_{ads}) derived from oxygen vacancy and better catalyst reducibility. The ozone concentration remarkably decreased after the introduction of catalysts, especially for CoO_x-CeO_2 catalysts. The key process parameters including pulsed power, gaseous hourly space velocity (GHSV), relative humidity (RH), and oxygen content were optimized by response surface methodology (RSM) integrated central composite design (CCD). The proposed optimization model displayed satisfactory correlation between the predicted and experimental results. GHSV was the most significant parameter affecting the energy yield, whereas the CO_x selectivity was mainly influenced by the pulsed power. Besides, the possible toluene degradation pathway in plasma-catalysis over CoO_x-CeO_2 was proposed according to the identification of gaseous intermediates and organic aerosol using FT-IR and GC-MS.

1. Introduction

Volatile organic compounds (VOCs) released from a variety of industrial sites are considered as one of the primary air pollution expect for NO_x and SO_2, and extremely harmful to human's health because of the formation of photochemical smog and ground-level ozone [1,2]. Catalytic destruction of volatile organic compounds (VOCs) is considered as one of the most promising technologies used to decrease their emission due to high products selectivity as well as low production of secondary pollutants [3]. In general, catalysts employed for VOCs degradation can be classified into noble metal and transition metal oxide catalysts. Compared with noble metal catalysts, transition metal oxide

(such as Co_3O_4, Fe_2O_3, MnO_2, CeO_2, CuO, NiO, and Cr_2O_3) catalysts have attracted widespread attention owing to their high reactivity, low cost, and environmentally-friendly [4,5]. Among the transition metal oxide catalysts, cobalt oxide is considered as a promising active catalyst for gaseous contaminant degradation including CO, NO_x and VOCs because of its weak oxygen bond strength and high turnover frequency for oxidation-reduction reactions [6–8]. Bai et al. [7] and Gennequin et al. [9] reported the excellent catalytic activity of cobalt-containing catalysts towards toluene oxidation. It is also known that an appropriate catalyst support with porous structure benefits to increase the dispersion of active metal component and improve its catalytic activity [10–12]. Supported metal oxides on γ-Al_2O_3 catalysts have been widely

used and proven to be efficient for VOCs oxidation [10,12]. Besides, ceria-containing oxides have arouse widespread concern as a promoter in heterogeneous catalytic reactions because of its remarkable oxygen storage capacity and distinct redox couple of Ce^{3+}/Ce^{4+} [11,12]. The introduction of Ce into transition metal oxides has been proven to further promote the oxygen mobility as well as the redox properties. Co_3O_4-CeO_2 catalysts have been found to be active for CO and VOCs oxidation due to their catalytic synergistic effect between Co and Ce species [12,13]. Wang et al. [13] reported that Co-Ce composite oxide catalyst had a highly efficient activity for chlorinated VOCs, which can be ascribed to the increased content of Co^{2+} species and oxygen vacancies due to the incorporation of Ce. However, a great disadvantage of the catalytic oxidation system is their lack of activity below 250 °C, which have significant issues associated with low temperature conditions where very poor VOCs degradation efficiency is achieved [13–15].

In recent years, non-thermal plasma (NTP) is considered to be an attractive option to traditional thermal activation reaction because plenty of energetic electrons, ions, radicals, and excited species can overcome the catalyst activation barrier by excitation and enable catalysts to be efficient in pollutants conversion at low temperature [16–20]. Consequently, plasma-assisted catalysis has drawn widespread interest owing to the integrated advantages of quick and low-temperature reaction from NTP and high mineralization efficiency from catalysis. Plasma-assisted catalysis has been proven to be efficient for the removal of a variety of pollutants at ambient temperature, even for the abatement of refractory aromatic hydrocarbon [21–24]. The VOCs degradation performance is mainly connected with the position of catalysts either by introducing the catalyst in plasma zone (in plasma-catalysis, IPC) or placing the catalyst downstream the discharge plasma reactor (post plasma-catalysis, PPC) [24–28]. In these two combination ways, the gas-phase reaction and catalyst surface reaction induce a synergistic effect, which contributes to a significantly higher degradation and mineralization performance than NTP alone [22–26]. Compared to IPC process, the underling mechanism of PPC process is more straightforward because the plasma and catalysis are independent, and the reaction parameters can be optimized and controlled separately. Our previous work observed that PPC process could decompose O_3 more effectively than IPC process, which significantly improved the completely oxidation of target VOC and organic intermediates [11]. In PPC process, the primary function played by NTP is changing the gas composition before reacting with the catalysts [22,29]. The plasma can enrich the gas composition with highly reactive species and convert the macromolecular or refractory VOCs into micromolecular or easier removed substances for catalysis.

In PPC system for VOCs degradation, the development of an efficient plasma reactor is critical to optimize the gas composition fed into the catalysis. We have previously reported on plasma degradation of VOC using SLDBD plasma with three-electrode arrangement, and remarkable better decomposition and energy performance were obtained in the SLDBD reactor with three-electrode configuration compared to traditional surface DBD (SDBD) reactor with two-electrode configuration because of more homogeneous distribution of chemical active species on the dielectric surface under identical energy condition [30–32]. Despite SLDBD proved capacity to destruct VOC, the degradation efficiency and energy yield still need to be further improved. Several researchers have reported works on how to expand the plasma region as well as facilitate the decomposition of VOC molecules. It was obvious that the combination of multiple plasma cells in series can greatly enhance the VOCs degradation efficiency. Harling et al. [33] pointed out that a multistage plasma system consisted of three DBD plasma cells presented a significant increase in the decomposition of toluene and ethylene. However, a separate power supply was also required to excite each plasma cell, which would raise the investment and operation cost. In the work of Malik et al. [34], a coupled surface DBD reactor was developed by employing multiple interconnected electrodes in the same space, and higher NO conversion efficiency was achieved

using the coupled SDBD than single one.

Inspired by the above-mentioned studies, we presently focus on the post plasma-catalytic oxidation of toluene in an enlarged pulsed SLDBD reactor based on multi-electrodes configuration over a series of CoO$_x$-CeO$_2$ catalysts at ambient temperature. To the best of our knowledge, the VOC degradation over CoO$_x$-CeO$_2$ supported catalysts activated by NTP at ambient temperature and atmospheric pressure is still very limited. Also, special attention has been focus on the influence of the Co/Ce molar ratio on the physicochemical characteristics of CoO$_x$-CeO$_2$ catalysts and their catalytic properties towards VOC degradation in PPC system, which was systematically studied in terms of catalyst characterization techniques, such as Brunauer–Emmett–Teller (BET), X-ray powder diffraction (XRD), scanning electron microscope (SEM), high resolution transmission electron microscopy (HRTEM), X-ray photoelectron spectroscopy (XPS), and hydrogen temperature-programmed reduction (H$_2$-TPR). The synergistic catalytic mechanism between Co and Ce species during PPC process was specifically discussed. Moreover, RSM-CCD model has been employed to further optimize the key process parameters (pulsed power, GHSV, RH, and oxygen content) in terms of energy yield and CO$_x$ selectivity, which is expected to be an effective technology for the optimization and prediction of plasma-catalytic degradation of VOC.

2. Experimental

2.1. Experiments with the multi-SLDBD plasma reactor

The experimental setup of toluene degradation in PPC system was described in Fig. 1(a), which comprised of a VOC generation system, a multi-SLDBD plasma reactor, a power supply system, and an analytical equipment system. The SLDBD with multiple-electrode configuration was an enlarged version of the reactor utilized for toluene removal in our previous work [30–32], as shown in Fig. 1(b). Briefly, a pair of quartz plates opposite to each other served as the dielectric layer, and the distance between the two dielectric layers was fixed at 10 mm. The six discharge electrodes (electrode #1) were made of aluminum foil sheet of 50 μm thickness, 8 mm width, and 80 mm length. Herein, three of them were embedded on the top dielectric layer, and the other three were embedded on the bottom dielectric layer. Each side of the electrode #1 were placed with a same size aluminum foil sheet that acted as the counter electrode (electrode #3). The ground electrode (electrode #2), made of copper foil (180 mm × 80 mm), was installed on the opposite surface of the dielectric barrier. The inter-electrode distance between the electrode #1 and electrode #3 was kept at 20 mm. The total area between all the discharge electrodes and counter electrodes, which was equivalent to the area covered by the plasma, was approximately 192 cm^2.

A pulsed power supply that can deliver positive high-voltage pulses in the range of 0–35 kV with 50 Hz repetition rate was applied on the discharge electrode to ignite plasma. Surface streamer channels appear close to the edge of the discharge electrode and form a narrow plasma region. For the purpose of prolonging the plasma region, the counter electrodes were driven by DC voltage to form an additional electric field between the discharge electrode and the counter electrode. The surface streamer channels can further extend covering the entire dielectric surface caused by a sufficient electric field between the discharge and counter electrodes. The pulsed voltage waveform was monitored using a high-voltage probe (Tektronix P6015A). The power delivered to the discharge reactor was computed by measuring the current i_1 and i_2 on the ground and counter electrodes using two current probes (Tektronix TCP202), respectively. The waveforms of voltage and current were recorded by a digital storage oscilloscope (Tektronix DPO2014) with a bandwidth of 100 MHz. The instantaneous total power ($P_{total}(t)$) was calculated by using the sum of the power provided by both the positive pulsed and negative DC power supplies [35].
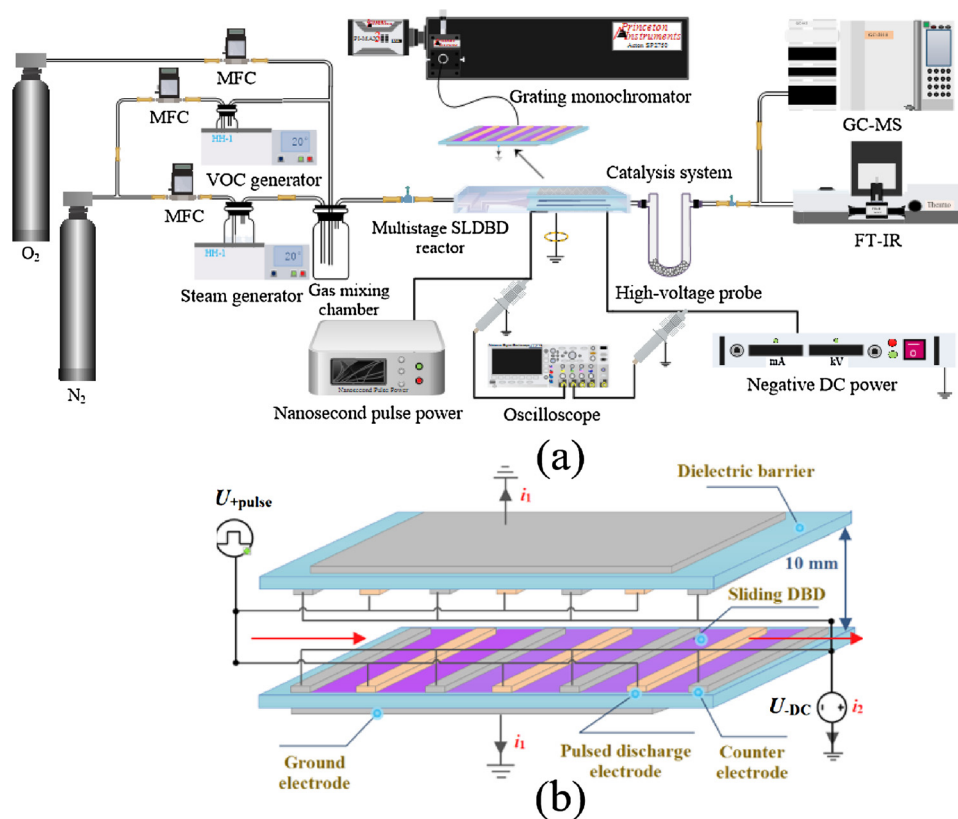
Fig. 1. Schematic diagrams of (a) the experimental setup and (b) the multi-SLDBD reactor.

$$P_{\text{total}} = \left[\int_0^T U_{\text{+pulse}}(t) \times i_1(t)dt \right] \times f + \left[\int_0^T U_{\text{-DC}} \times i_2(t)dt \right] \tag{1}$$

Fig. S1 shows typical voltage waveform, currents waveforms measured on the ground electrode (i_1) and counter electrode (i_2), and the instantaneous total power as a function of the discharge time. As presented in Fig. S1a, the pulsed voltage increases up to 18 kV after less than 90 ns, while the pulsed current i_1 reaches the maximum 36.9 A after approximately 70 ns. Current i_2 can also be detected on the counter electrode at about 200 ns, which is caused by the drift of ionized species generated from pulsed electrode towards the counter electrode due to the increased electric field between the above two electrodes. The result of Fig. S1b indicates that the majority of consumed power is supplied by the positive pulsed high-voltage, however, the negative DC voltage is only responsible for a fraction of the dissipated power.

Toluene-containing air was prepared by bubbling "synthetic air" through a thermostatic water bath containing toluene. The initial concentration and flow rate of the toluene-containing air were fixed at 300 ppm and 3 L/min, respectively. Toluene was quantified by GC (Shimadzu GC-2010) with a FID. The RH of air-containing toluene was controlled by adjusting the water bath temperature, and which was monitored by a humidity tester (Rotronic HP22-A). The inlet and outlet gas stream were online analyzed using FTIR (Nicolet 6700, USA) in the range of 1000-4000 cm^{-1} with a resolution of 0.5 cm^{-1}, combined with a 2.4 m gas cell. The organic aerosols accumulated on the reactor and the catalyst surface after long-time discharge were collected by acetone and qualitatively identified using GC-MS (Agilent 7000B, USA). Ozone quantification was performed by iodometry. All the experiments were carried out more than thrice and the total error resulted from repeat measurements was within ± 5%. The plasma gas temperature of multi-SLDBD was calculated by the optical emission spectra (OES) of $N_2(C^3\Pi_u \rightarrow B^3\Pi_g)$ using the Specair software. The OES emitted from the plasma zone were measured by a spectrograph (Princeton Instruments,

Action SP2750, USA). A U-type reactor filled with the prepared catalysts was placed downstream from the multi-SLDBD reactor, and the post plasma-catalytic degradation experiments were performed at ambient temperature. The calculation methods of toluene degradation efficiency, CO_x selectivity, energy yield (*EY*) and GHSV were detailed described in Text S1 of SI.

2.2. Catalyst preparation and characterization

The CoO_x and CeO_2 supported catalysts with 10 wt% loading were prepared by the impregnation method on γ-Al_2O_3 support using Co $(NO_3)_2$ and $Ce(NO_3)_2$ as precursor, respectively. The CoO_x-CeO_2 supported catalyst with total loading of 10 wt% of cobalt and cerium was prepared following the same procedure of CoO_x and CeO_2 samples, which was labeled as CoO_x-CeO_2 (*m:n*). *m:n* represented the Co/Ce molar ratio. The prepared samples were dried at 105 °C overnight and subsequently calcined at 450 °C for 4 h in a muffle furnace.

The catalyst characterization methods were detailed described in Text S2 of SI.

2.3. Experimental design and procedure of response surface methodology (RSM)

In order to optimize the process parameters affecting the VOC degradation reaction in PPC system, four experimental parameters including pulsed discharge power (A), GHSV (B), RH (C) and oxygen content (D) have been investigated using a five-level CCD defined under RSM, while energy yield (Y1) and CO_x selectivity (Y2) were considered as response factors. Table S1 presents the range and levels of the four process parameters. Table S2 shows the experimental design matrix of the CCD for VOC degradation process. As presented in Table S2, a five-level CCD model with 30 experimental sets was designed to optimize the independent process parameters.

Table 1
Physicochemical properties and surface composition of CoO_x, CeO_2, and CoO_x-CeO_2 supported catalysts with different Co/Ce molar ratios.

Sample	S_{BET}[a] (m²/g)	D_{pore}[b] (nm)	V_p[b] (cm³/g)	$Ce^{3+}/$ $(Ce^{3+} + Ce^{4+})$[c]	$Co^{2+}/$ $(Co^{2+} + Co^{3+})$[c]	$O_{ads}/$ $(O_{ads} + O_{latt})$[c]	Lattice parameters[d] (Å)
γ-Al_2O_3	273.5	5.53	0.486	——	——	——	——
CoO_x	115.8	5.68	0.304	——	43.4	52.1	——
CoO_x-CeO_2 (3:1)	158.5	5.33	0.364	26.9	57.6	67.6	5.3925
CoO_x-CeO_2 (1:1)	155.4	5.33	0.353	20.1	54.2	62.7	5.3929
CoO_x-CeO_2 (1:3)	155.8	5.32	0.347	26.4	55.3	65.3	5.3939
CeO_2	155.2	5.58	0.340	14.8	——	61.6	5.4022

[a] BET method.
[b] BJH method.
[c] The internal standard method with the aid of relative sensitivity factors.
[d] The lattice parameters are calculated by Jade program based on the CeO_2 (111) crystal plane.

3. Result and discussion

3.1. Catalysts characterizations

Table 1 summarizes the main physicochemical properties of the CoO_x, CeO_2, and CoO_x-CeO_2 supported catalysts with various Co/Ce molar ratio, including specific surface area (S_{BET}), average pore volume (V_{pore}), and average pore diameter (D_{pore}). S_{BET} of γ-Al_2O_3 is 273.5 m²/g, while those of the CoO_x, CeO_2, and CoO_x-CeO_2 supported catalysts varies from 115.8 to 157.5 m²/g, suggesting that the incorporation of Co and Ce species reduces the surface area of catalyst. Besides, it is observed that S_{BET} increases obviously after incorporating Ce into CoO_x. V_{pore} of all the prepared samples is in the range of 0.304-0.364 cm³/g except for γ-Al_2O_3 support, which follows a similar trend with S_{BET}. Among all the prepared catalyst, CoO_x-CeO_2 (3:1) exhibits the largest S_{BET} and V_{pore} of 158.5 m²/g and 0.364 cm³/g, respectively.

XRD has been utilized to determine the nature of the phases present in the catalyst samples, as shown in Fig. 2. For CeO_2 supported catalysts, the diffraction peaks at $2\theta = 28.5°$, 33.1°, 47.5°, and 56.3° are identified corresponding to the typical face-centered cubic fluorite structure of CeO_2 (JCPDS file No.43-1002) [36]. The CoO_x sample exhibits the diffraction peaks at 19.0°, 31.3°, 36.8°, 44.8°, 55.6°, 59.4°, 65.2°, and 77.3°, which correspond to the (111), (220), (311), (400), (422), (511), (440), and (533) planes of the spinel Co_3O_4 phase (JCPDS Card no. 42-1467) [5]. XRD patterns of CoO_x-CeO_2 supported catalysts presents the combination of CeO_2 and Co_3O_4 phases. In addition, the lattice parameters have been calculated by Jade program based on the CeO_2 (111) crystal plane, as shown in Table 1. It is clear that the lattice parameters of CoO_x-CeO_2 samples are lower than pure CeO_2, indicating that the cobalt ions are incorporated into CeO_2 lattice to form a Co_3O_4-CeO_2 solid solution because the ionic radius of Co^{3+} (0.061 nm) or Co^{2+} (0.075 nm) is smaller than that of Ce^{4+} (0.101 nm) [37]. This

replacement also results in the lattice distortion of the solid solution and the formation of oxygen vacancies. Similar results were also reported by Akram et al. [38] and Wang et al. [39].

The morphology characteristics of the CoO_x and CoO_x-CeO_2 supported samples are performed by SEM, and the results are presented in Fig. S2. In the SEM image of CoO_x, particles of different sizes are agglomerated and form block-like nanoclusters on the surface of catalyst (Fig. S2a). CoO_x-CeO_2 exhibits a more homogeneous appearance, with particles of smaller grain size dispersed on the catalyst surface (Fig. S2b). The EDX spectra result confirms the existing of Co and Ce with atomic percentage of 1.25% and 0.47%, respectively (Fig. S2d). The actual Co/Ce molar ratio is similar to the theoretical value. HRTEM has also been conducted to confirm the structure characteristics of lattice fringes of the CoO_x-CeO_2 sample, as shown in Fig. 3. Lattice fringes in HRTEM image of CeO_2 (Fig. 3a) are 0.31 nm corresponding to the (111) plane. Pure CoO_x presents a well-organized lattice fringes with a spacing of 0.46 nm, which can be assigned to the (111) plane of Co_3O_4 (Fig. 3c). CoO_x-CeO_2 (3:1) shows the lattice fringes with spacing of 0.31 nm and 0.24 nm, respectively, corresponding to the spacing of CeO_2 (111) and Co_3O_4 (311) planes. It's worth noting that an interconnected structure of lattice fringes can be observed in binary CoO_x-CeO_2 (3:1) (Fig. 3b), implying that interaction occurs between Co and Ce species. High angle annular dark field mapping (HAADF) micrographs and EDX mapping images are presented in Fig. 3d, e, and f. It is clear that Co and Ce species are homogeneously dispersed on the surface of $CoO_x CeO_2$ (3:1) catalyst, which is beneficial for oxygen storage and mobility and thus improves the catalytic activity for VOC oxidation.

XPS experiments are performed to determine the chemical states of the surface Co, Ce, and O in CoO_x-CeO_2 supported catalysts, and the corresponding results are presented in Fig. 4. The XPS spectra of Co2p for the CoO_x and CoO_x-CeO_2 samples present two main peaks centered at around 795.4 and 780.1 eV, which are ascribed to $Co2p_{1/2}$ and $Co2p_{3/2}$ spin-orbit-split double peak of Co_3O_4 spinel, respectively (Fig. 4a) [40,41]. The $Co2p_{1/2}$ and $Co2p_{3/2}$ peaks can be fitted and deconvoluted into four peaks. The peaks centered at 780.8 and 796.4 eV are assigned to Co^{2+}, while those at 779.6 and 794.9 eV are attributed to Co^{3+}. The $Co^{2+}/(Co^{2+} + Co^{3+})$ molar ratio for CoO_x-CeO_2 (3:1), CoO_x-CeO_2 (1:1), and CoO_x-CeO_2 (1:3) samples are 57.6%, 54.2%, and 55.3%, respectively, which is higher than 43.4% for CoO_x. The incorporation of Ce into CoO_x leads to generating more cobalt cations with a lower valence state (Co^{2+}) to maintain electronic neutrality, which favors the formation of more oxygen vacancies on the catalyst surface. Similar results were also reported by Zhu et al. [6] and Wang et al. [13]

As shown in Fig. 4b, the XPS spectra of Ce 3d exhibits the spin-orbit doublets of Ce $3d_{5/2}$ and Ce $3d_{3/2}$, marked as v_0, v_1, v_2, v_3, u_0, u_1, u_2, and u_3. The signals v_0, v_2, v_3, u_0, u_2, and u_3 are assigned to Ce^{4+} state, while signals v_1 and u_1 are ascribed to Ce^{3+} state [42]. As shown in Table 1, the molar ratio of $Ce^{3+}/(Ce^{3+} + Ce^{4+})$ for all the samples varies from
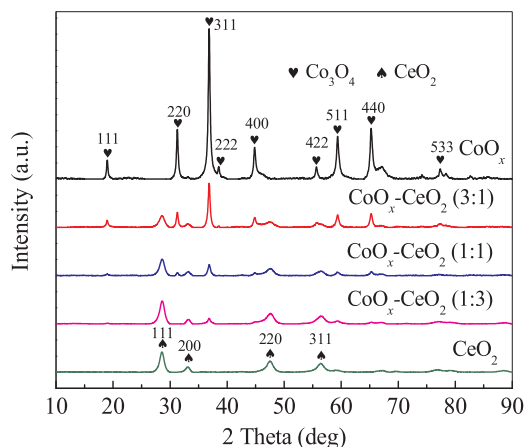
Fig. 2. XRD patterns of CoO_x, CeO_2, and CoO_x-CeO_2 supported catalysts.

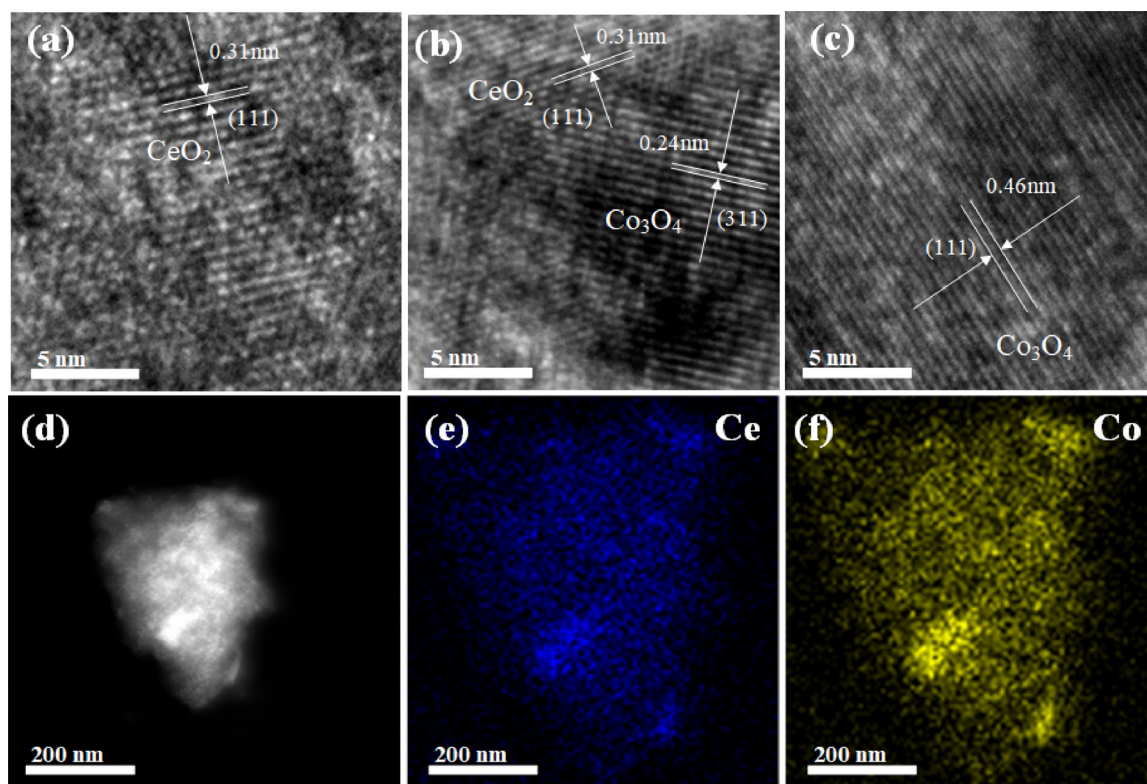**Fig. 3.** HRTEM images of (a) CeO_2, (b) CoO_x-CeO_2 (3:1), and (c) CoO_x, (d) HAADF micrograph of CoO_x-CeO_2 (3:1), EDX mapping images of (e) Ce and (f) Co elements of CoO_x-CeO_2 (3:1).

14.8% to 26.9%, suggesting that the primary valence of surface Ce species on the catalyst is Ce^{4+} oxidation state. It is also seen that the CoO_x-CeO_2 samples show higher $Ce^{3+}/(Ce^{3+}+Ce^{4+})$ ratio compared to CeO_2 sample, while decreases in the order of CoO_x-CeO_2 (3:1) > CoO_x-CeO_2 (1:3) > CoO_x-CeO_2 (1:1). It is well recognized that higher relative content of Ce^{3+} can results in generating more oxygen vacancies due to charge compensation, which in turn favors the destruction of VOC and intermediates molecules [14,43].

The O 1s XPS spectra of the CoO_x, CeO_2, and CoO_x-CeO_2 samples are presented in Fig. 4c, which can be deconvoluted into two components. The peak located in the range of 529.4–530.0 eV can be assigned to lattice oxygen (O^{2-}, defined as O_{lat}), while the peak centered at approximately 531.3 eV is ascribed to surface adsorbed oxygen (O_2^{2-} or O-, defined as O_{ads}) derived from carbonates and oxygen vacancy [44]. Compared to CoO_x, a shift of O_{latt} peak towards lower binding energy can be found on CoO_x-CeO_2, demonstrating that the chemical environment of lattice oxygen is greatly affected by the doping of Ce species. The lower binding energy of O_{latt} can make the surface oxygen more unstable, which is favorable for the catalytic degradation of toluene and intermediates adsorbed on the catalyst surface [45]. Moreover, as presented in Table 1, the molar ratio of $O_{ads}/(O_{ads}+O_{lat})$ on the surface of CoO_x-CeO_2 samples is obviously higher than that on the CoO_x surface. It is generally believed that the presence of oxygen vacancies greatly favors the generation of O_{ads} on the catalyst surface, which is propitious to catalytic oxidation reaction due to its higher mobility than O_{lat} [46,47]. The consumed oxygen vacancies can be replenished by adjacent gas phase active oxygen species (O^*) formed via ozone decomposition reaction [48,49].

The catalyst redox activity is also crucial for catalytic oxidation reaction. H_2-TPR experiment was carried out to evaluate the redox capacity of all the catalyst samples, and the result is displayed in Fig. S3. The H_2-TPR profile of CeO_2 is characterized by a low intensity and broad peak with a maximum at 750.4 °C, which can be assigned to the consumption H_2 by bulk CeO_2 [50]. It has been reported that the

introduction of catalyst support could reduce the reduction temperature, and the decreased value depends mainly on the property of catalyst and the dispersion level of cerium oxide [51,52]. The H_2-TPR profile of the CoO_x sample presents two broad peaks at 531.9 and 602.5 °C, ascribed to the reduction process of Co_2O_3 to CoO and CoO to metallic cobalt, respectively [53]. Compared with the CoO_x sample, the corresponding reduction peaks shift to a lower temperature region after Ce doping. Especially, the high temperature peak become a shoulder peak for all the CoO_x-CeO_2 samples, suggesting that the existence of Ce promote the reducibility of Co^{3+} to Co^{2+} [54]. Better catalyst reducibility is expected to play a key role in catalytic activity towards VOC degradation. According to the temperature of reduction peak, the catalysts reducibility declines in the sequence of CoO_x-CeO_2 (3:1) > CoO_x-CeO_2 (1:3) > CoO_x-CeO_2 (1:1) > CoO_x, which is in agreement with the results from XPS analysis.

3.2. Toluene degradation performance in plasma-catalysis system

In the present experiment, the PPC process has been performed without additional heating equipment. For the purpose of estimating the gas temperature of the multi-SLDBD plasma, the experimental spectra of nitrogen bands (N_2(C-B)) are compared with the simulated one to determine the rotational temperature by means of specair software [55,56]. It is logical to hypothesis that the rotational temperature of atmospheric discharge is in equilibrium with its translational temperature. Therefore, the rotational temperature can be regarded as an indicator of plasma gas temperature (T_{gas}). The evolution of T_{gas} as a function of *SIE* during the multi-SLDBD plasma is displayed in Fig. 5. The standard deviation of the experimental results is represented by error bars. As shown in the embedding graph of Fig. 5, there is good overlap between the simulation results and the experimental data, indicating a best-fit T_{gas} of 362 K at *SIE* of 431 J/L. It is noteworthy that T_{gas} increases slightly with *SIE*. As *SIE* increases from 211.4 to 809.2 J/L, T_{gas} ranges from 348 ± 5 to 362 ± 5 K, suggesting that thermal
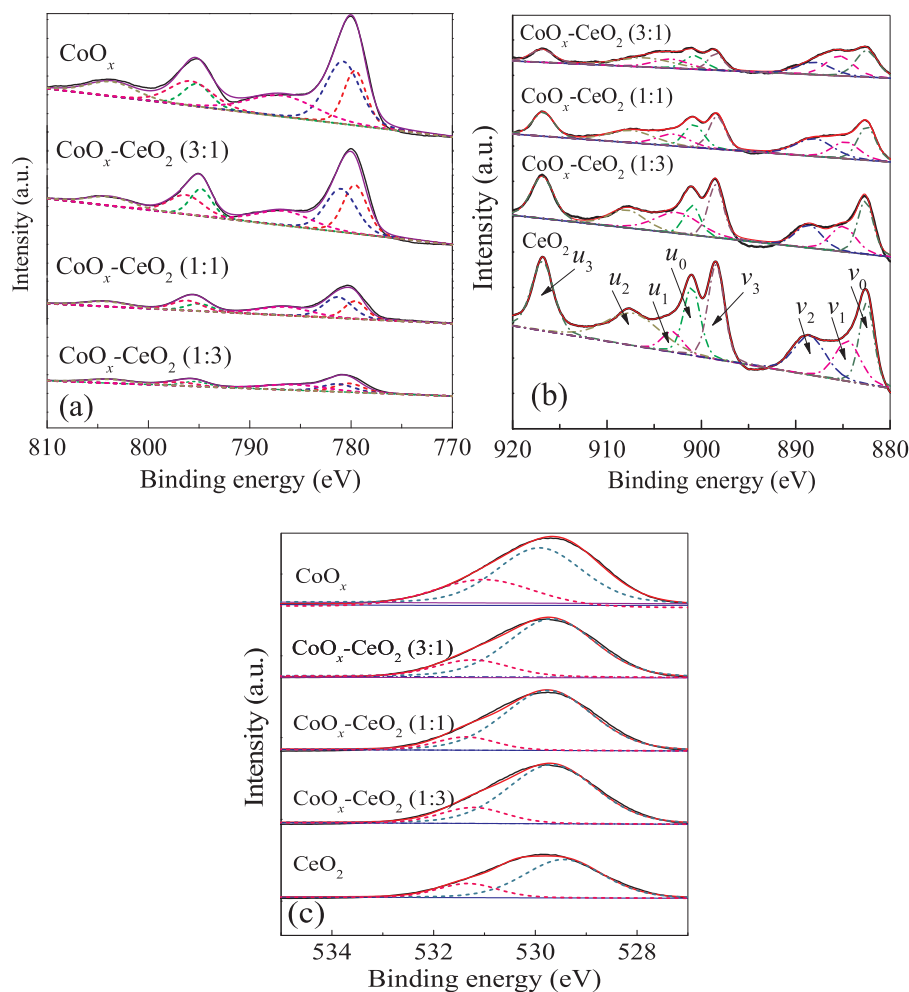
Fig. 4. (a) Co 2p, (b) Ce 3d, and (c) O 1s XPS spectra of the CoO_x, CeO_2, and CoO_x-CeO_2 supported catalysts.

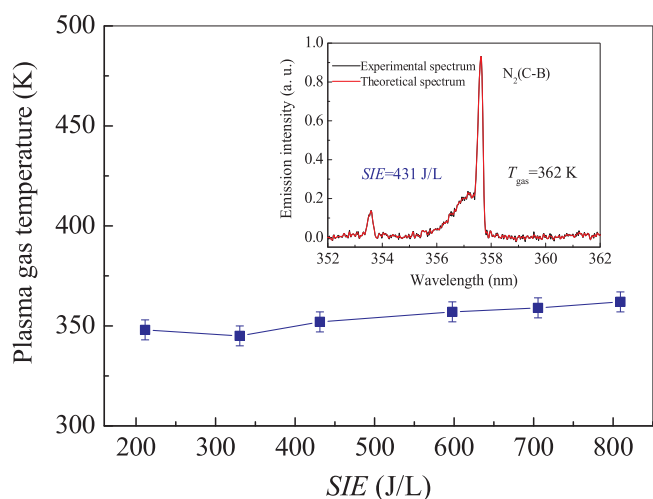**Fig. 5.** Plasma gas temperature as a function of *SIE* during the multi-SLDBD plasma measured by OES of N_2(C-B).

activation of the catalysts is unlikely the cause of the improved performance for toluene degradation.

Fig. 6 presents the toluene degradation efficiency, CO_x selectivity, energy yield, and O_3 concentration as a function of *SIE* in plasma and PPC processes over CoO_x, CeO_2, and CoO_x-CeO_2 supported catalysts. As shown in Fig. 6a and b, both the toluene degradation efficiency and CO_x

selectivity increase significantly as *SIE* increases, irrespective of the catalysts used. In the absence of catalyst, the toluene degradation efficiency increases from 18.0% to 65.2% as *SIE* increases from 211 to 809 J/L, and the corresponding CO_x selectivity increases from 22.0% to 70.5%. It is commonly believed that more energetic electrons are generated under higher energy condition, contributing to the formation of more chemical reactive species such as excited atoms, molecules, free radicals, and ions, and thus the degradation and mineralization of toluene is improved. The combination of the plasma and catalyst leads to a significant enhancement in degradation, mineralization, and energy performance than the plasma process alone. At the same *SIE*, the degradation efficiency of toluene, CO_x selectivity, and energy yield decrease in the order of CoO_x-CeO_2 (3:1) > CoO_x-CeO_2 (1:3) > CoO_x-CeO_2 (1:1) > CeO_2 > CoO_x > γ-Al_2O_3 support $>$ plasma alone, which is closely consistent with the results acquired by XPS and H_2-TPR analyses. At 809 J/L, the toluene degradation efficiency and CO_x selectivity increase from 65.2% to 92.1% and 70.5 to 92.3% when CoO_x-CeO_2 (3:1) is introduced downstream the plasma region, and the corresponding energy yield increased by approximately 41%. Therefore, the PPC process combining multi-SLDBD and CoO_x-CeO_2 catalyst is advantageous to destroy VOC and organic intermediates from the perspective of both degradation and energy performance.

The remarkable catalytic activity of CoO_x-CeO_2 (3:1) for toluene degradation and mineralization in PPC process could be ascribed to several factors that are closely correlated. According to the XPS analysis, CoO_x-CeO_2 (3:1) sample exhibits higher O_{ads} content than the other samples owing to the interaction between Co and Ce species. O_{ads} is proven to be favorable for catalytic oxidation process due to its
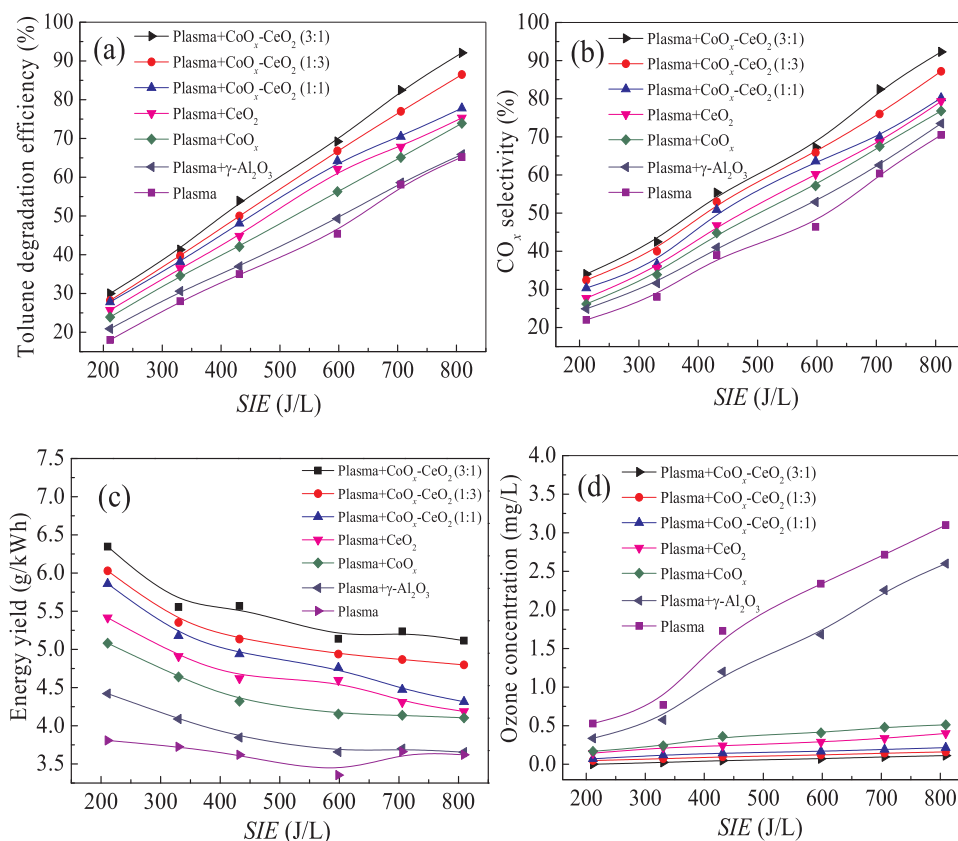
Fig. 6. Effect of *SIE* on plasma and post plasma-catalytic degradation of toluene: (a) degradation efficiency; (b) CO_x selectivity; (c) energy yield; (d) O_3 concentration.

higher mobility than O_{lat}, which contributes to superior oxidation efficiency of toluene and organic intermediates. Moreover, the presence of Ce^{3+}/Ce^{4+} redox couple is beneficial to increase the mobility of oxygen species and thus facilitates the reduction of Co^{2+}/Co^{3+}. As a result, the redox cycle between Co and Ce cations ($Co^{2+} + Ce^{4+} \leftrightarrow Co^{3+} + Ce^{3+}$) occurs on the CoO_x-CeO_2 supported catalyst and the electron transfer can be promoted as followed:

$$Ce^{4+} - O^{2-} - Co^{3+} + e^- \leftrightarrow Ce^{4+} - O^{2-} - Co^{2+} \leftrightarrow Ce^{3+} - O^{2-} - Co^{3+}$$
$$\leftrightarrow Ce^{4+} - O^{2-} - Co^{3+} + e^-$$

[6,57,58]. The oxidation reduction cycle leads to a decrease in the energy required for the electron transfer between Co and Ce species, improving the catalyst reducibility and enhancing its catalytic activity towards VOC oxidation [57]. In addition, it is worth noting that S_{BET}, V_{pore}, and D_{pore} of the CoO_x-CeO_2 catalysts are significantly lower than that of pure γ-Al_2O_3 support (Table 1), indicating that the surface structure of catalyst is not the critical factor affecting the plasma-catalytic reaction for VOC degradation. Similar conclusion was also reported by Pan et al. [59]. The adsorbed toluene and organic intermediates on the catalyst surface can be further oxidized by adjacent O^* from O_3 decomposition and O_{ads} derived from oxygen vacancies, which results in an improved degradation and mineralization performance [59–61]. Subsequently, the consumed oxygen vacancies in the catalyst can be supplemented by O^* from ozone decomposition [48,49].

As presented in Fig. 6d, all the samples present capacity to decompose ozone, even for pure γ-Al_2O_3. Ozone has been reported to decompose to active oxygen species (O^*) and O_2 on the catalyst surface according to the following reactions (Eqs. (2)–(4)), where * denotes the active sites of the catalyst [60,61].

$$O_3 + ^* \rightarrow O_2 + O^* \tag{2}$$

$$O^* + O_3 \rightarrow O_2 + O_2^* \tag{3}$$

$$O_2^* \rightarrow O_2 + ^* \tag{4}$$

In terms of the reactivity toward VOCs oxidation, O^* is a more chemically active species compared to ozone. Therefore, it would be more favorable for toluene oxidation if ozone is decomposed to O^* before reacting with toluene and organic fragments. The ozone decomposition efficiency follows the same trend as the toluene degradation efficiency and CO_x selectivity at any given *SIE*, being highest for CoO_x-CeO_2 (3:1).

The long-time stability experiment has been carried out to evaluate the durability of the CoO_x-CeO_2 in PPC system at room temperature, and the results were presented in Fig. 7. The experiment has been performed for 4 days with a daily startup-closedown. Toluene-containing air with initial concentration of 300 ppm was degraded by plasma catalysis for 8 h a day at *SIE* of 809 J/L. As shown in Fig. 7, both the degradation efficiency and CO_x selectivity almost maintained constant during 4 days treatment, indicating that CoO_x-CeO_2 supported catalyst displays excellent catalytic activity and stability for the
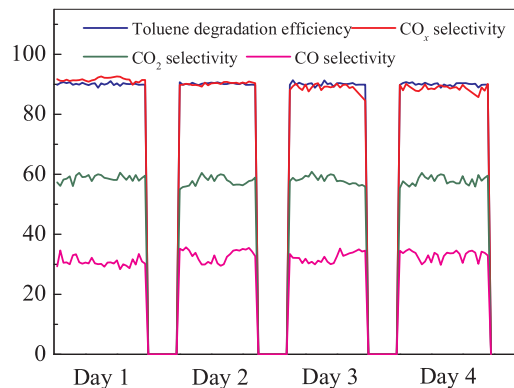

Fig. 7. Long-time stability experiments over CoO_x-CeO_2 (3:1) supported catalysts in post plasma-catalysis system.

degradation and mineralization of aromatic hydrocarbon with the assistance of multi-SLDBD plasma.

3.3. Optimization of the post plasma-catalytic degradation process

3.3.1. Model statistical analysis

To optimize the key operating parameters of the PPC process over CoO_x-CeO_2 catalyst, the run of 30 experimental sets were employed for response surface modeling. Each experiment was performed thrice to ensure the adequacy of the proposed model. Based on the fitting of 30 groups of experimental data, the regression equations for predicting the energy yield and CO_x selectivity in post plasma-catalysis process are presented as follow:

$$Y1 \text{ (energy yield)} = 2.85 - 0.18 \text{ A} + 0.3 \text{ B} - 0.003 \text{ C} - 0.018 \text{ D} - 0.070 \text{ AB} - 0.066 \text{ AC} - 0.039 \text{ AD} - 0.037 \text{ BC} - 0.067 \text{ BD} - 0.074 \text{ CD} - 0.01 \text{ A}^2 + 0.15 \text{ B}^2 - 0.053 \text{ C}^2 - 0.073 \text{ D}^2 \tag{5}$$

$$Y2 \text{ (CO}_x \text{ selectivity)} = 59.67 + 10.17 \text{ A} - 6 \text{ B} - 0.25 \text{ C} + 5.83 \text{ D} - 0.12 \text{ AC} + 0.13 \text{ AD} + 0.25 \text{ BD} + 0.13 \text{ CD} + 0.063 \text{A}^2 + 0.19 \text{ B}^2 - 3.81 \text{ C}^2 + 0.81 \text{ D}^2 \tag{6}$$

In the above equations, positive and negative coefficients imply favorable and unfavorable effects on the respond factors (energy yield and CO_x selectivity), respectively. Analysis of variance (ANOVA) was performed to assess the importance and of the developed quadratic model (p-values < 0.05), as summarized in Table 2. As shown in Table 2, the models are statistically significant in fitting the actual data with the Fischer's F-test (F-value) for both energy yield (46.5) and CO_x selectivity (253.2) at a probability value (p-value) < 0.0001. The model's veracity can also been validated by the lack of fit (LOF) F-value. The inapparent LOF F-values for energy yield (1.2) and CO_x selectivity (0.23) indicate the excellent fitting of the proposed model to predict the responding factors. Low values of coefficient of variance (C.V.) for energy yield (2.84%) and CO_x selectivity (5.39%) confirm high repeatability of the experimental results [62,63]. In addition, the precision ratios reach 29.44 and 56.573 for energy yield and CO_x selectivity, respectively, implying that the proposed models have high fitting degree and sufficient signal-to-noise ratios [64]. The high correlation coefficient (R^2) values of 0.9775 and 0.9958 for energy yield and CO_x selectivity indicate that the regression models are significant. The

models' reliability for predicting energy yield and CO_x selectivity of the PPC process can also been confirmed by the adjusted R^2 values of 0.9565 and 0.9919, respectively [65].

Fig. 8 shows the normal probability plot of the experimental results and predicted versus actual values for energy yield and CO_x selectivity, respectively. It is clear that most of the data are close to a straight line, implying good adequacy of the regression models for both energy yield and CO_x selectivity. The results in Fig. 8c and d demonstrate an excellent correlation between the experimental and the predicted values of the models for energy yield and CO_x selectivity, indicating that the models are valid and significant.

3.3.2. The mutual effects of the process parameters on responses

The mutual effects of the four experimental parameters (pulsed power, GHSV, RH, and oxygen content) on the energy yield and CO_x selectivity in the PPC system were analyzed using the 3D response surface, as presented in Figs. 9 and 10. It is seen from Figs. 9a and 10 a that the pulsed power has a significant impact on energy yield and CO_x selectivity. The energy yield decreases with increasing pulsed power, despite of high mineralization efficiency under high energy conditions. That is because more energy in plasma is consumed due to vibrational and electronic excitation of gas molecules, and utilized for O_3 and NO_x formation as the discharge power increases, which results in a decrease in energy yield [66].

The results in Figs. 9a and 10 a show that as GHSV increases, conspicuous monotonic increase and decrease can be observed in energy yield and CO_x selectivity, respectively. The increased energy yield with GHSV can be ascribed to more amount of toluene per unit volume of catalyst, which results in more violent collision between toluene molecules with chemical reactive species. However, the decreased CO_2 selectivity with increasing GHSV may be caused by low residence time of toluene and organic intermediates on the active sites of catalysts.

As shown in Fig. 9b and 10 b, both the energy yield and CO_x selectivity increase first and then decrease as RH increases from 5 to 65% in PPC process. This result can be explained by the following aspects: 1) The addition of water vapor is favorable for ˙OH generation, and thus the degradation and mineralization of toluene and organic intermediates is improved; 2) However, more high-energy electrons could be captured by electronegative H_2O molecules with further increasing RH, which results in a decrease in reactive species generation; 3) On the

Table 2
ANOVA results of response surface quadratic models.

| Source	Energy yield (Y1)			CO_x selectivity (Y2)		
	Sum of Square	F-Value	p-Value	Sum of Square	F-Value	p-Value
Model	4.28	46.50	< 0.0001	4627.88	253.20	< 0.0001
A	0.79	120.42	< 0.0001	2480.67	1900.09	< 0.0001
B	2.16	328.38	< 0.0001	864.00	661.79	< 0.0001
C	2.67×10^{-3}	0.041	0.8431	1.50	1.15	0.3007
D	8.07×10^{-3}	1.23	0.2856	816.67	625.53	< 0.0001
AB	0.078	11.92	0.0036	0.000	0.000	1.0000
AC	0.070	10.68	0.0052	0.25	0.19	0.6679
AD	0.024	3.65	0.0753	0.25	0.19	0.6679
BC	0.022	3.42	0.0842	0.000	0.000	1.0000
BD	0.073	11.08	0.0046	1.00	0.77	0.3953
CD	0.087	13.23	0.0024	0.25	0.19	0.6679
A^2	2.74×10^{-3}	0.42	0.5282	0.11	0.082	0.7784
B^2	0.61	92.27	< 0.0001	0.96	0.74	0.4036
C^2	0.076	11.49	0.0040	398.68	305.37	< 0.0001
D^2	0.14	21.92	0.0003	18.11	13.87	0.0020
Residual	0.099			19.58		
Lack of Fit	0.070	1.2	0.4469	6.25	0.23	0.9755
Pure error	0.029			13.33		
Cor Total	4.38			4647.47		
R^2 = 0.9775		C.V.% = 2.84		R^2 = 0.9958		C.V.% = 1.99
Adjusted R^2 = 0.9565				Adjusted R^2 = 0.9919		
Precision ratios = 29.440				Precision ratios = 56.573		
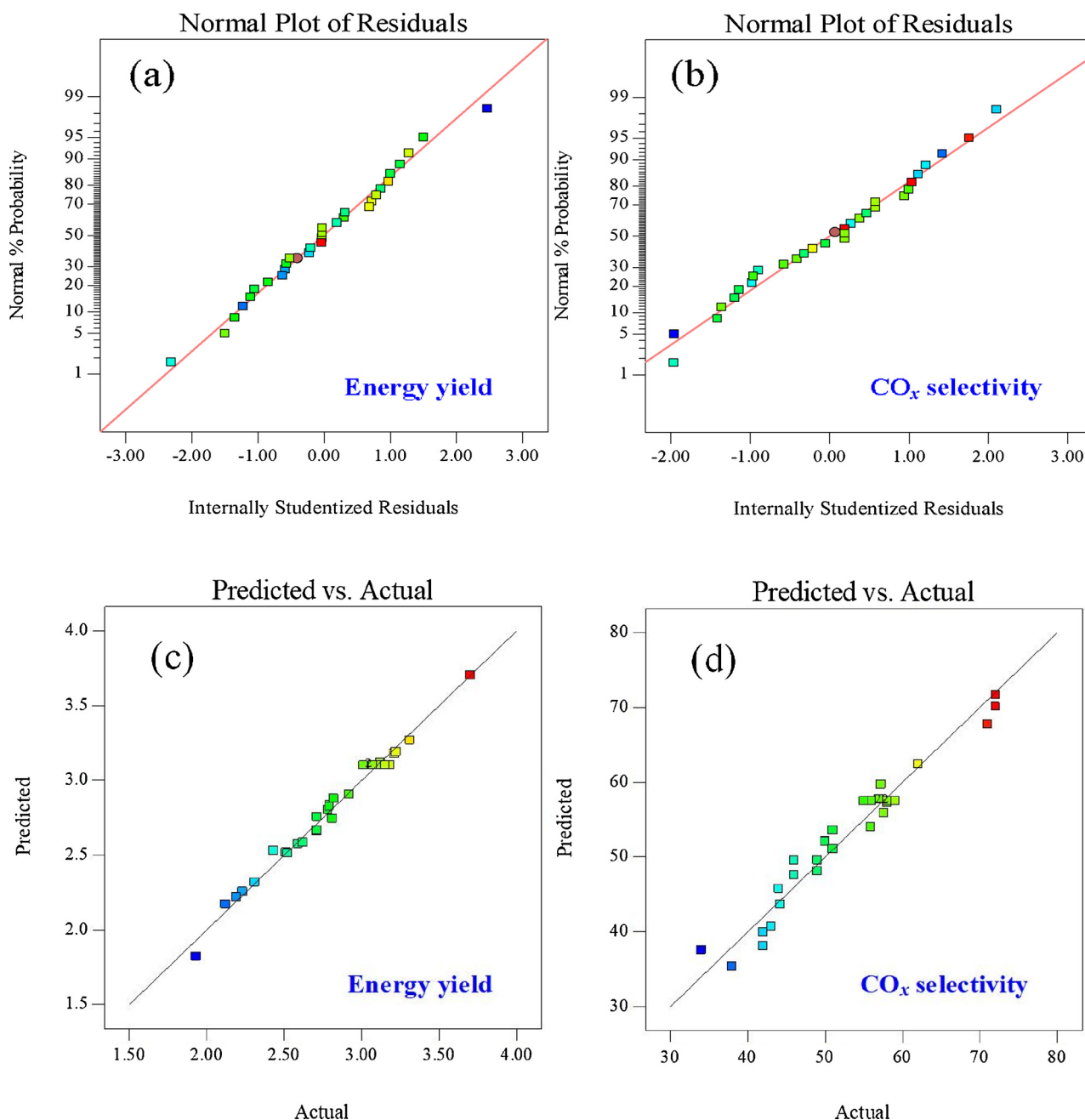
Fig. 8. The normal probability plots of the experimental results for (a) energy yield and (b) CO_x selectivity, predicted versus actual values for (c) energy yield and (d) CO_x selectivity.

other hand, excess H_2O molecules will occupy the active sites of the catalysts, which leads to decreasing the catalytic activity for toluene degradation [11,67].

The results in Fig. 9c exhibits that the energy yield increases first and then decreases as the oxygen content increases. That is because higher oxygen content favors the formation of oxygen-containing active species (O_3, O, etc.), resulting in better degradation and energy performance. However, as the oxygen content further increases, more reactive nitrogen-containing active species quench through collision with reactive oxygen species, which cannot be utilized for toluene degradation and leads to a decrease in energy yield [68]. As presented in Fig. 10c, CO_x selectivity exhibits a monotonous increase as the oxygen content increases, suggesting that more amount of oxygen-containing active species formed at higher oxygen content that are beneficial to the mineralization of toluene and organic intermediates.

The contribution of each experiment parameter on the reaction performance was also evaluated using the response surface plots (Fig. 9 and 10). As for energy yield in PPC system, the contribution of GHSV is observed to be dominant with the highest F-value of 328.38, followed by pulsed power with F-value of 120.42, whereas the effects of RH and oxygen content on energy yield are insignificant. Pulsed power has more pronounced effect on CO_x selectivity, followed by GHSV and oxygen content, respectively. However, the influence of RH on CO_x selectivity is limited, suggesting that the post plasma-catalytic degradation of toluene is available and feasibility under a broad range of RH conditions.

The optimal conditions are determined after comprehensive consideration of both energy and mineralization performance. Based on these, highest energy yield and CO_x selectivity of 5.1 g/kWh and 67.2% were achieved for toluene degradation in post plasma-catalysis process
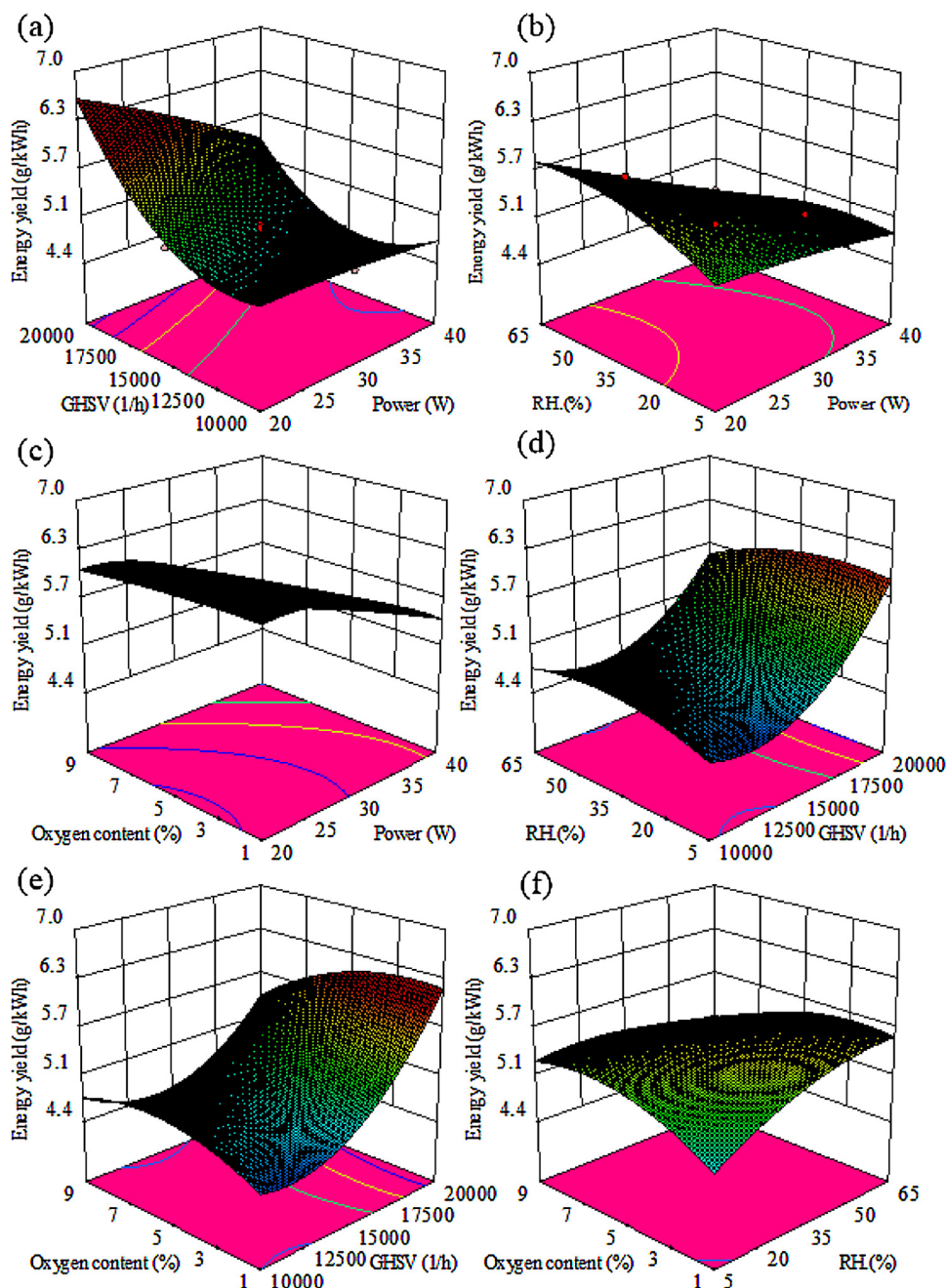
Fig. 9. The 3D response surface plots of the interaction of pulsed power, GHSV, RH, and oxygen content on energy yield.

at approximately 33 W, 17500 h^{-1}, 28% and 7% for pulsed power, GHSV, RH, and oxygen content, respectively.

3.4. Products identification and degradation mechanism analysis

Further experiments have been carried out to analyze the gas composition of the exhaust gas after plasma and post plasma-catalytic treatment using FTIR, and the results are presented in Fig. 11. It is clear that the FTIR bands between 2800 and 3100 cm^{-1}, belonging to the vibrational C−H stretching of toluene, decline after plasma treatment. At the same time, the bands of gas phase CO, CO_2, H_2O, and formic acid appear, indicating that toluene has been destroyed by the multi-SLDBD plasma and at least partially mineralized into CO_2 and H_2O. Additionally, in order to analyze the possible degradation pathway by post plasma-catalysis over CoO_x-CeO_2, the organic aerosols deposited on the plasma reactor wall and on the catalyst surface after long-time

treatment were extracted by acetone and subsequently identified by GC–MS.

As shown in Table S3, the domain organic intermediates identified after plasma treatment includes acetic acid, 4-hydroxy-4-methyl-2-pentanone, 6-hydroxy-2-hexanone, benzaldehyde, allylbenzene, 3-methylfuran-2,5-dione, phenylmethanol, and 3-methyldihydrofuran-2,5-dione. It is generally believed that VOCs degradation in air plasma process is primary induced by energetic electron impact and reactions with discharge generated chemical reactive species including ·O, ·N, ·OH, and $N_2(A^3\Sigma_u^+)$. The reaction rate constant of energetic electrons with toluene is 1×10^{-6} cm^3 mol^{-1}·s^{-1}, which is much higher than that of O_3, ·O, and ·OH [69–71]. Consequently, the energetic electrons attack may contribute to the initial chemical bonds rupture of toluene. The chemical reactive species in gas phase can also participate in toluene destruction, particularly in the mineralization reaction of organic intermediates. The possible toluene degradation pathways by multi-
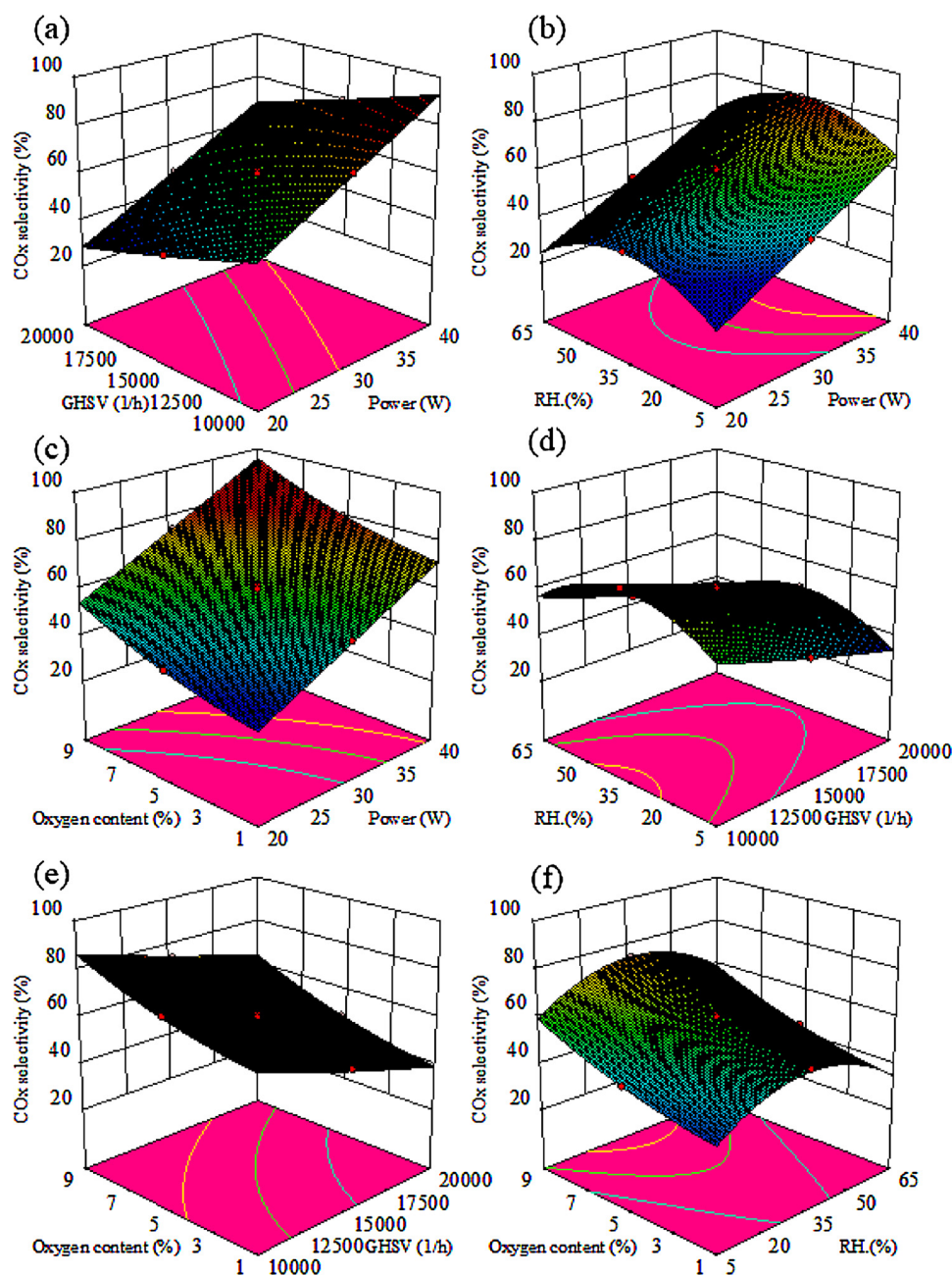
Fig. 10. The 3D response surface plots of the interaction of pulsed power, GHSV, RH, and oxygen content on CO_x selectivity.

SLDBD plasma are presented in Fig. 12.

The C−H bond dissociation energy in methyl and benzene ring, and C−C bond dissociation energy between benzene ring and methyl group are 3.7, 4.3, and 4.4 eV, respectively, which is much lower than the dissociation energy of C−C bond in benzene ring (5.0–5.3 eV) and C═C bond in benzene ring (5.5 eV) [72,73]. Consequently, the initial toluene destruction pathways are via breaking the C−H bonds in methyl and benzene ring, and C−C bonds between methyl group and benzene ring, forming benzyl and phenyl radicals [74,75]. The above radicals can be further oxidized to generate benzaldehyde, allylbenzene, and phenylmethanol in the presence of oxygen-containing reactive species ($\cdot$O, $\cdot$OH, and $\cdot$O$_2$). In addition, 3-methylfuran-2,5-dione and 3-methyldihydrofuran-2,5-dione were detected in this work. However, their generation mechanisms are still very speculative. Wagner et al. [76] reported that hydroxyl could replace a hydrogen atom which was adjacent to a methyl group on benzene ring, forming aromatic-OH adducts. Aromatic-OH adducts can further convert to hydroxyl

cyclohexadienyl type peroxy radicals with $\cdot$O$_2$ [77]. The unstable intermediates can form reactive peroxide bicyclic products, and which can be further oxidized into linear organic intermediates such as acetic acid, 6-hydroxy-2-hexanone, and 4-hydroxy-4-methyl-2-pentanone in the ring opening reactions. The subsequent reactions are proceeded by series of oxidation steps by the attack of oxygen-containing reactive species, leading to the generation of final products (CO_2 and H_2O). However, it's worth noting that only formic acid can be identified in the exhaust gas because of the detection limit of FTIR. The methyl group makes a great contribution to the generation of formaldehyde and formyl group in gas phase, which further oxidized into formic acid, and finally mineralized to CO_2 and H_2O in the presence of oxygen-containing reactive species.

The catalytic surface reactions also contribute to the destruction of organic intermediates adsorbed on the catalyst surface. As presented in Table S4, 9 types of organic substances were detected on the surface of CoO_x-CeO_2 supported catalyst, including 2-ethoxyprop-2-en-1-ol, acetic
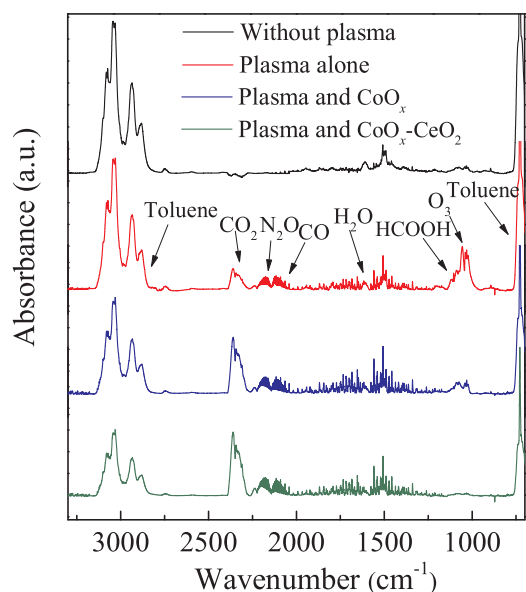
Fig. 11. FTIR spectra of gas composition after plasma and post plasma-catalytic treatment over CoO_x and CoO_x-CeO_2 supported catalysts at *SIE* of 598 J/L.

anhydride, 2-(2-oxocyclopent-3-en-1-yl) acetaldehyde, cyclopet-4-ene-1,3-dione, 2-ethyl-5-methylfuran, benzaldehxde, acethyl 2-acetox-yacetate, phenol, diethyl malonate, and 5-ethoxydihydrofuran-2(3H)-one. The plasma-catalytic surface reaction mechanism on the CoO_x-CeO_2 supported catalyst is presented in Fig. 13. The reactive species produced close to the interface between the CoO_x-CeO_2 catalysts would spread on the catalyst surface and involve in the plasma-catalytic surface reaction. The redox cycle between Co and Ce cations ($Co^{2+} + Ce^{4+} \leftrightarrow Co^{3+} + Ce^{3+}$) occurs on the surface of CoO_x-CeO_2 catalysts, which can reduce the energy required for the electron transfer and facilitates oxygen mobility, which is beneficial to improve the reducibility of catalysts [57,58]. The toluene and aromatic intermediates adsorbed on the surface of CoO_x-CeO_2 catalysts can react with adjacent O_{ads} from oxygen vacancies and O^* from O_3 decomposition, and deeply oxidized into liner organic intermediates including 2-ethoxyprop-2-en-1-ol, acetic anhydride, acethyl 2-acetoxyacetate, and diethyl malonate, ultimately, mineralized to CO_2 and H_2O at room temperature [78]. Subsequently, the consumed oxygen vacancies in the catalyst can be supplemented by adjacent O^* from ozone decomposition [48,49].

4. Conclusion

In the present work, effective degradation of toluene in gas phase has been achieved in a PPC system using pulsed multi-electrode SLDBD over CoO_x-CeO_2 supported catalysts. Toluene degradation and
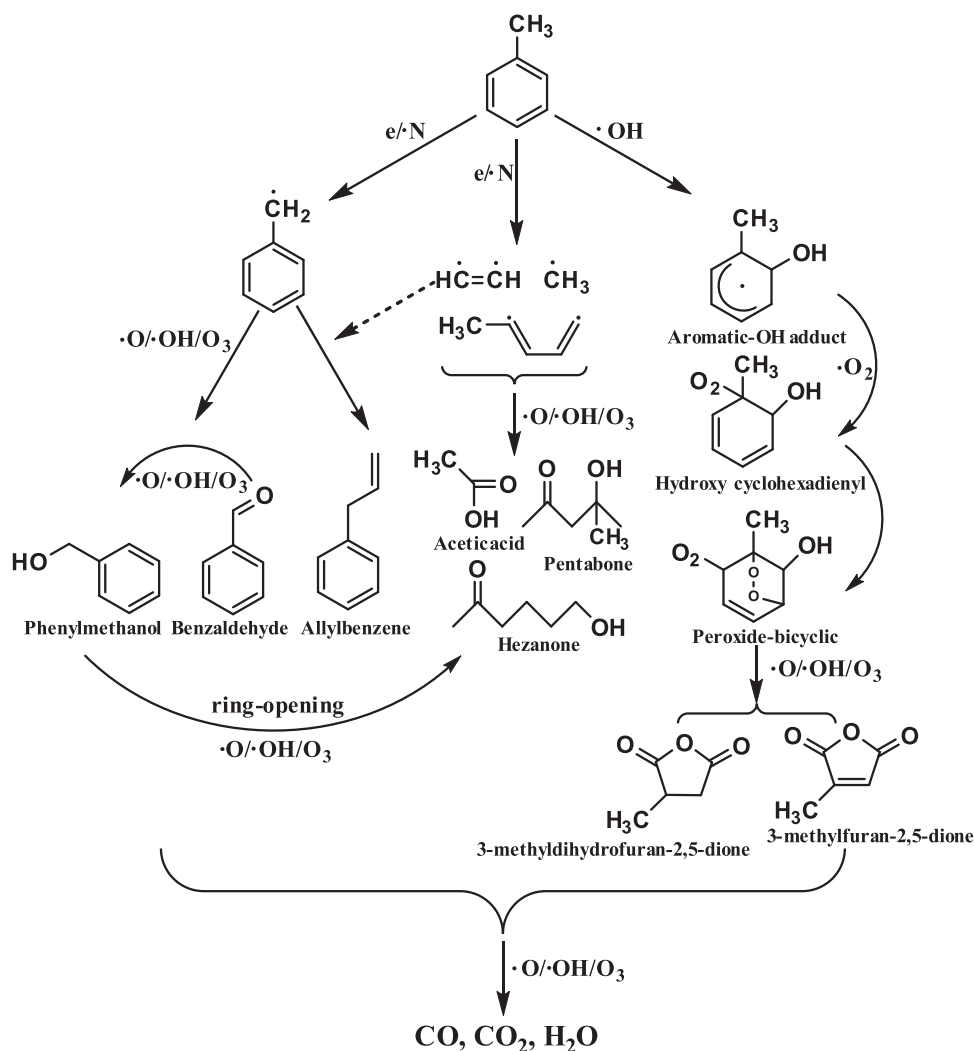

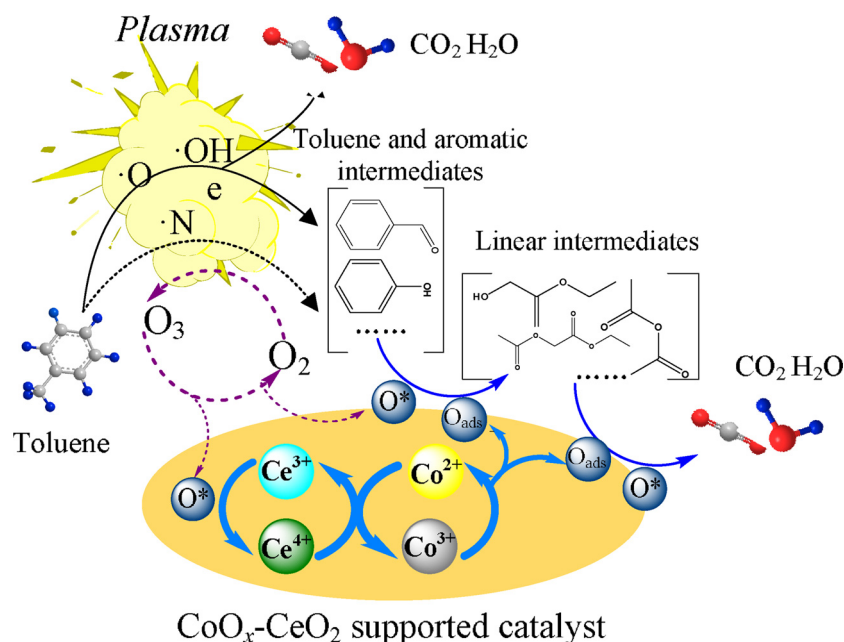**Fig. 12.** The possible degradation pathways of toluene by multi-SLDBD plasma.

Fig. 13. Post plasma-catalytic reaction mechanism on the CoO_x-CeO_2 supported catalysts.

mineralization performance are significantly improved after the combination of catalysts than plasma-only system. Moreover, the presence of catalyst significantly suppresses the formation of the decomposition products and discharge byproducts. The incorporation of Ce into CoO_x supported catalyst promotes the catalytic activity, and CoO_x-CeO_2 (3:1) displays the best toluene degradation efficiency, CO_x selectivity, and O_3 decomposition efficiency. The oxygen mobility and O_3 decomposition are remarkably improved due to high content of O_{ads} and excellent reducibility of CoO_x-CeO_2 (3:1) supported catalysts, which favors the enhanced catalytic activity for toluene degradation and mineralization. RSM-CCD models have been employed to evaluate the contribution of different process parameters (pulsed power, GHSV, RH, and oxygen content) and their interaction on energy yield as well as CO_x selectivity in PPC process. The analysis of the optimization model indicates that the pulsed power has more pronounced effect on CO_x selectivity, whereas GHSV play a dominant role in energy yield. The optimal mineralization efficiency and energy yield of 67.2% and 5.1 g/kWh could be achieved for post plasma-catalytic degradation of toluene at approximately 33 W, 17500 h^{-1}, 28% and 7% for pulsed power, GHSV, RH, and oxygen content, respectively.

Declaration of Competing Interest

The authors declare that they have no known competing financial interests or personal relationships that could have appeared to influence the work reported in this paper.

Acknowledgments

Appendix A. Supplementary data

Supplementary material related to this article can be found, in the online version, at doi:https://doi.org/10.1016/j.apcatb.2019.118061.

References

[1] J.H. Park, A.H. Goldstein, J. Timkovsky, S. Fares, R. Weber, J. Karlik, R. Holzinger, Active atmosphere-ecosystem exchange of the vast majority of detected volatile organic compounds, Science 341 (2013) 643–647.

[2] X. Zhu, S. Liu, Y. Cai, X. Gao, J. Zhou, C. Zheng, X. Tu, Post-plasma catalytic removal of methanol over Mn–Ce catalysts in an atmospheric dielectric barrier discharge, Appl. Catal. B 183 (2016) 124–132.

[3] W. Si, Y. Wang, S. Zhao, F. Hu, J. Li, A facile method for in situ preparation of the MnO_2/$LaMnO_3$ catalyst for the removal of toluene, Environ. Sci. Technol. 50 (2016) 4572–4578.

[4] L.F. Liotta, G.D. Carlo, G. Pantaleo, G. Deganello, Catalytic performance of Co_3O_4/ CeO_2 and Co_3O_4/CeO_2–ZrO_2 composite oxides for methane combustion: influence of catalyst pretreatment temperature and oxygen concentration in the reaction mixture, Appl. Catal. B: Environ. 70 (2007) 314–322.

[5] Z. Chen, S. Wang, W. Liu, X. Gao, D. Gao, M. Wang, S. Wang, Morphology-dependent performance of Co_3O_4 via facile andcontrollable synthesis for methane combustion, Appl. Catal. A 525 (2016) 94–102.

[6] X. Zhu, S. Zhang, Y. Yang, C. Zheng, J. Zhou, X. Gao, Xin Tu, Enhanced performance for plasma-catalytic oxidation of ethyl acetateover $La_{1-x}Ce_xCoO_{3+\delta}$ catalysts, Appl. Catal. B 213 (2017) 97–105.

[7] G. Bai, H. Dai, J. Deng, Y. Liu, F. Wang, Z. Zhao, W. Qiu, C.T. Au, Porous Co_3O_4 nanowires and nanorods: highly active catalysts for the combustion of toluene, Appl. Catal. A 450 (2013) 42–49.

[8] J. Jansson, A.E.C. Palmqvist, E. Fridell, M. Skoglundh, L. Osterlund, P. Thormahlen, V. Langer, On the catalytic activity of Co_3O_4 in low-temperature CO oxidation, J. Catal. 211 (2002) 387–397.

[9] C. Gennequin, R. Cousin, J.-F. Lamonier, S. Siffert, A. Aboukaïs, Toluene total oxidation over Co supported catalysts synthesised using "memory effect" of Mg–Al hydrotalcite, Catal. Commun. 9 (2008) 1639–1643.

[10] J. Li, G. Lu, G. Wu, D. Mao, Y. Wang, Y. Guo, Promotional role of ceria on cobaltosic oxide catalyst for low-temperature CO oxidation, Catal. Sci. Technol. 2 (2012) 1865–1871.

[11] N. Jiang, J. Hu, J. Li, K. Shang, N. Lu, Y. Wu, Plasma-catalytic degradation of benzene over Ag-Ce bimetallic oxide catalysts using hybrid surface/packed-bed discharge plasmas, Appl. Catal. B 184 (2016) 355–363.

[12] S. Lin, G. Su, M. Zheng, D. Ji, M. Jia, Y. Liu, Synthesis of flower-like Co_3O_4–$CeO2$ composite oxide and its application to catalytic degradation of 1,2,4-trichlorobenzene, Appl. Catal. B 123–124 (2012) 440–447.

[13] C. Wang, C. Zhang, W. Hua, Y. Guo, G. Lu, S. Gil, A. Giroir-Fendler, Catalytic oxidation of vinyl chloride emissions over Co-Ce composite oxide catalysts, Chem. Eng. J. 315 (2017) 392–402.

[14] S. Gil, J. Garcia-Vargas, L. Liotta, G. Pantaleo, M. Ousmane, L. Retailleau, A. Giroir-Fendler, Catalytic oxidation of propene over Pd catalysts supported on CeO_2, TiO_2, Al_2O_3 and M/Al_2O_3 oxides (M = Ce, Ti, Fe, Mn), Catalysts 5 (2015) 671.

[15] B. de Rivas, N. Guillén-Hurtado, R. López-Fonseca, F. Coloma-Pascual, A. García-García, J.I. Gutiérrez-Ortiz, A. Bueno-LópezActivity, Selectivity and stability of praseodymium-doped CeO_2 for chlorinated VOCs catalytic combustion, Appl. Catal. B 121–122 (2012) 162–170.

[16] X. Wang, Y. Gao, S. Zhang, H. Sun, J. Li, T. Shao, Nanosecond pulsed plasma assisted dry reforming of CH_4: the effect of plasma operating parameters, Appl. Energy 243 (2019) 132–144.

[17] Y. Cao, X. Qian, Y. Zhang, G. Qu, T. Xia, X. Guo, H. Jia, T. Wang, Decomplexation of EDTA-chelated copper and removal of copper ions by non-thermal plasma oxidation/alkaline precipitation, Chem. Eng. J. 362 (2019) 487–496.

[18] B. Sun, D. Liu, F. Iza, S. Wang, A. Yang, Z. Liu, M. Rong, X. Wang, Global model of an atmospheric-pressure capacitive discharge in helium with air impurities from 100 to 10000 ppm, Plasma Sources Sci. Technol. 28 (2019) 035006.

[19] Y. Gao, S. Zhang, H. Sun, R. Wang, X. Tu, T. Shao, Highly efficient conversion of methane using microsecond and nanosecond pulsed spark discharges, Appl. Energy 226 (2018) 534–545.

[20] Z. Chen, D. Liu, H. Xu, W. Xia, Z. Liu, D. Xu, M. Rong, M.G. Kong, Decoupling analysis of the production mechanism of aqueous reactive species induced by a helium plasma jet, Plasma Sources Sci. Technol. 28 (2019) 025001.

[21] A.M. Harling, V. Demidyuk, S.J. Fischer, J.C. Whitehead, Plasma-catalysis destruction of aromatics for environmental clean-up: effect of temperature and configuration, Appl. Catal. B 82 (2008) 180–189.

[22] H.L. Chen, H.M. Lee, S.H. Chen, M.B. Chang, S.J. Yu, S.N. Li, Removal of volatile organic compounds by single-stage and two-stage plasma catalysis systems: a review of the performance enhancement mechanisms, current status, and suitable applications, Environ. Sci. Technol. 43 (2009) 2216–2227.

[23] H. Guo, N. Jiang, H. Wang, K. Shang, N. Lu, J. Li, Y. Wu, Enhanced catalytic performance of graphene-TiO$_2$ nanocomposites for synergetic degradation of fluoroquinolone antibiotic in pulsed discharge plasma system, Appl. Catal. B 248 (2019) 552–566.

[24] M.T. Nguyen Dinha, J.M. Giraudona, A.M. Vandenbrouckeb, R. Morentb, N. De Geyterb, J.F. Lamoniera, Post plasma-catalysis for total oxidation of trichloroethylene over Ce−Mn based oxides synthesized by a modified "redox-precipitation route", Appl. Catal. B 172–173 (2015) 65–72.

[25] A.M. Vandenbroucke, M. Mora, C. Jiménez-Sanchidrián, F.J. Romero-Salguero, N. De Geyter, C. Leys, R. Morent, TCE abatement with a plasma-catalytic combined system using MnO$_2$ as catalyst, Appl. Catal. B 156 (2014) 94–100.

[26] M.T. Nguyen Dinh, J.-M. Giraudon, J.-F. Lamonier, A. Vandenbroucke, N. De Geyter, C. Leys, R. Morent, Plasma-catalysis of low TCE concentration in air using LaMnO$_{3+\delta}$ as catalyst, Appl. Catal. B 147 (2014) 904–911.

[27] H. Guo, N. Jiang, H. Wang, N. Lu, K. Shang, J. Li, Y. Wu, Degradation of antibiotic chloramphenicol in water by pulsed discharge plasma combined with TiO$_2$/WO$_3$ composites: mechanism and degradation pathway, J. Hazard. Mater. 371 (2019) 666–676.

[28] H. Guo, N. Jiang, H. Wang, N. Lu, K. Shang, J. Li, Y. Wu, Pulsed discharge plasma assisted with graphene-WO$_3$ nanocomposites for synergistic degradation of antibiotic enrofloxacin in water, Chem. Eng. J. 372 (2019) 226–240.

[29] E.C. Neyts, K. Ostrikov, M.K. Sunkara, A. Bogaerts, Plasma catalysis: synergistic effects at the nanoscale, Chem. Rev. 115 (2015) 13408–13446.

[30] N. Jiang, L. Guo, C. Qiu, Y. Zhang, K. Shang, N. Lu, J. Li, Y. Wu, Reactive species distribution characteristics and toluene destruction in the three-electrode DBD reactor energized by different pulsed modes, Chem. Eng. J. 350 (2018) 12–19.

[31] N. Jiang, C. Qiu, L. Guo, K. Shang, N. Lu, J. Li, Y. Wu, Discharge and optical characterizations of nanosecond pulse sliding dielectric barrier discharge plasma for volatile organic compound degradation, J. Phys. D Appl. Phys. 50 (2017) 155206.

[32] N. Jiang, C. Qiu, L. Guo, K. Shang, N. Lu, J. Li, Y. Zhang, Y. Wu, Plasma-catalytic destruction of xylene over Ag-Mn mixed oxides in a pulsed sliding discharge reactor, J. Hazard. Mater. 369 (2019) 611–620.

[33] A.M. Harling, D.J. Glover, J.C. Whitehead, K. Zhang, Novel method for enhancing the destruction of environmental pollutants by the combination of multiple plasma discharges, Environ. Sci. Technol. 42 (2008) 4546–4550.

[34] M.A. Malik, K.H. Schoenbach, R. Heller, Coupled surface dielectric barrier discharge reactor-ozone synthesis and nitric oxide conversion from air, Chem. Eng. J. 256 (2014) 222–229.

[35] S. Tang, N. Li, D. Yuan, J. Tang, X. Li, C. Zhang, Y. Rao, Comparative study of persulfate oxidants promoted photocatalytic fuel cell performance: simultaneous dye removal and electricity generation, Chemosphere 234 (2019) 658–667.

[36] E. Moretti, L. Storaro, A. Talon, M. Lenarda, P. Riello, R. Frattini, M. del Valle, M. de Yuso, A. Jimenez-Lopez, E. Rodriguez-Castellon, F. Ternero, A. Caballero, J.P. Holgado, Effect of thermal treatments on the catalytic behaviour in the CO preferential oxidation of a CuO–CeO$_2$–ZrO$_2$ catalyst with a flower-like morphology, Appl. Catal. B 102 (2011) 627–637.

[37] Z. Wang, G. Shen, J. Li, H. Liu, Q. Wang, Y. Chen, Catalytic removal of benzene over CeO$_2$-MnO$_x$ composite oxides prepared by hydrothermal method, Appl. Catal. B 138–139 (2013) 253–259.

[38] S. Akram, Z. Wang, L. Chen, Q. Wang, G. Shen, N. Han, Y. Chen, G. Ge, Low-temperature efficient degradation of ethyl acetate catalyzed by lattice-doped CeO$_2$–CoO$_x$ nanocomposites, Catal. Commun. 73 (2016) 123–127.

[39] J. Wang, M. Shen, J. Wang, J. Gao, J. Ma, S. Liu, CeO$_2$-CoO$_x$ mixed oxides: structural characteristics and dynamic storage/release capacity, Catal. Today 175 (2011) 65–71.

[40] Z. Wu, W. Ren, L. Wen, L. Gao, J. Zhao, Z. Chen, G. Zhou, F. Li, H. Cheng, Graphene anchored with Co$_3$O$_4$ nanoparticles as anode of lithium ion batteries with enhanced reversible capacity and cyclic performance, ACS Nano 4 (2010) 3187–3194.

[41] Z. Chen, S. Wang, W. Liu, X. Gao, D. Gao, M. Wang, S. Wang, Morphology-dependent performance of Co$_3$O$_4$ via facile andcontrollable synthesis for methane combustion, Appl. Catal. A 525 (2016) 94–102.

[42] J. Ma, C. Wang, H. He, Transition metal doped cryptomelane-type manganese oxide catalysts for ozone decomposition, Appl. Catal. B 201 (2017) 503–510.

[43] M. Ousmane, L.F. Liotta, G.D. Carlo, G. Pantaleo, A.M. Venezia, G. Deganello, L. Retailleau, A. Boreave, A. Giroir-Fendler, Supported Au catalysts for low-temperature abatement of propene and toluene, as model VOCs: support effect, Appl. Catal. B 101 (2011) 629–637.

[44] D. Jampaiah, S.J. Ippolito, Y.M. Sabri, B.M. Reddy, S.K. Bhargava, Highly efficient nanosized Mn and Fe codoped ceria-based solid solutions for elemental mercury removal at low flue gas temperatures, Catal. Sci. Technol. 5 (2015) 2913–2924.

[45] D. Zhang, L. Zhang, L. Shi, C. Fang, H. Li, R. Gao, L. Huang, J. Zhang, In situ supported MnO$_x$–CeO$_x$ on carbon nanotubes for the low-temperature selective catalytic reduction of NO with NH$_3$, Nanoscale 5 (2013) 1127–1136.

[46] Q. Dai, S. Bai, Z. Wang, X. Wang, G. Lu, Catalytic combustion of chlorobenzene over Ru-doped ceria catalysts, Appl. Catal. B: Environ. 126 (2012) 64–75.

[47] S.C. Kim, W.G. Shim, Catalytic combustion of VOCs over a series of manganese oxide catalysts, Appl. Catal. B: Environ. 98 (2010) 180–185.

[48] X. Zhu, X. Gao, X. Yu, C. Zheng, X. Tu, Catalyst screening for acetone removal in a single-stageplasma-catalysis system, Catal. Today 256 (2016) 108–114.

[49] S. Sultana, A.M. Vandenbroucke, M. Mora, C. Jiménez-Sanchidrián, F.J. Romero-Salguero, C. Leys, N. De Geyter, R. Morent, Post plasma-catalysis for trichloroethylene decomposition over CeO$_2$ catalyst: synergistic effect and stability test, Appl. Catal. B 253 (2019) 49–59.

[50] C. Norsic, J. Tatibouët, C. Batiot-Dupeyrat, E. Fourré, Non thermal plasma assisted catalysis of methanol oxidation on Mn, Ce and Cu oxides supported on γ-Al$_2$O$_3$, Chem. Eng. J. 304 (2016) 563–572.

[51] S.M. Saqer, D.I. Kondarides, X.E. Verykios, Catalytic oxidation of toluene over binary mixtures of copper, manganese and cerium oxides supported on γ-Al$_2$O$_3$, Appl. Catal. B 103 (2011) 275–286.

[52] G. Avgouropoulos, T. Ioannides, H. Matralis, Influence of the preparation method on the performance of CuO–CeO$_2$ catalysts for the selective oxidation of CO, Appl. Catal. B 56 (2005) 87–93.

[53] B. Meng, Z. Zhao, X. Wang, J. Liang, J. Qiu, Selective catalytic reduction of nitrogen oxides by ammonia over Co$_3$O$_4$ nanocrystals with different shapes, Appl. Catal. B Environ 129 (2013) 491–500.

[54] L.F. Liotta, G. Di Carlo, G. Pantaleo, G. Deganello, Co$_3$O$_4$/CeO$_2$ and Co$_3$O$_4$/CeO$_2$–ZrO$_2$ composite catalysts for methane combustion: correlation between morphology reduction properties and catalytic activity, Catal. Commun. 6 (2005) 329–336.

[55] J. Qiao, L. Zhang, D. Yang, Z. Jia, Y. Song, Z. Zhao, H. Yuan, Y. Xia, W. Wang, Temporal evolution of the relative vibrational population of N$_2$(C^3 II$_u$) and optical emission spectra of atmospheric pressure plasma jets in He mixtures, J. Phys. D Appl. Phys. 52 (2019) 285203.

[56] N. Jiang, C. Qiu, L. Guo, K. Shang, N. Lu, J. Li, Y. Wu, Improved performance for toluene abatement in a continuous-flow pulsed sliding discharge reactor based on three-electrode configuration, Plasma Chem. Plasma Process. 39 (2019) 227–240.

[57] M. Konsolakis, M. Sgourakis, S.A.C. Carabineiro, Surface and redox properties of cobalt–ceria binary oxides: on the effect of Co content and pretreatment conditions, Appl. Surf. Sci. 341 (2015) 48–54.

[58] Y. You, H. Chang, L. Ma, L. Guo, X. Qin, J. Li, J. Li, Enhancement of N$_2$O decomposition performance by N$_2$O pretreatment over Ce-Co-O catalyst, Chem. Eng. J. 347 (2018) 184–192.

[59] H. Pan, Y. Jian, C. Chen, C. He, Z. Hao, H. Liu, Z. Shen, Sphere-shaped Mn$_3$O$_4$ catalyst with remarkable low-temperature activity for methyl-ethyl-ketone combustion, Environ. Sci. Technol. 51 (2017) 6288–6297.

[60] H. Einaga, Y. Teraoka, A. Ogata, Catalytic oxidation of benzene by ozone over manganese oxides supported on USY zeolite, J. Catal. 305 (2013) 227–237.

[61] H. Einaga, N. Maeda, Y. Teraoka, Effect of catalyst composition and preparation conditions on catalyticproperties of unsupported manganese oxides for benzene oxidationwith ozone, Appl. Catal. B 142–143 (2013) 406–413.

[62] H. Guo, N. Jiang, H. Wang, K. Shang, N. Lu, J. Li, Y. Wu, Degradation of flumequine in water by pulsed discharge plasma coupled with reduced graphene oxide/TiO$_2$ nanocomposites, Sep. Purif. Technol. 218 (2019) 206–216.

[63] M. Pirsaheb, S. Moradi, M. Shahlaei, N. Farhadian, Application of carbon dots as efficient catalyst for the green oxidation of phenol: kinetic study of the degradation and optimization using response surface methodology, J. Hazard. Mater. 353 (2018) 444–453.

[64] B. Morero, E.S. Groppelli, E.A. Campanella, Evaluation of biogas upgrading technologies using a response surface methodology for process simulation, J. Cleaner Prod. 141 (2017) 978–988.

[65] S.K. Mondal, A.K. Saha, A. Sinha, Removal of ciprofloxacin using modified advanced oxidation processes: kinetics, pathways and process optimization, J. Cleaner Prod. 171 (2018) 1203–1214.

[66] M.F. Mustafa, X. Fu, Y. Liu, Y. Abbas, H. Wang, W. Lu, Volatile organic compounds (VOCs) removal in non-thermal plasma double dielectric barrier discharge reactor, J. Hazard. Mater. 347 (2018) 317–324.

[67] T. Chang, J. Lu, Z. Shen, Y. Huang, D. Lu, X. Wang, J. Cao, R. Morent, Simulation and optimization of the post plasma-catalytic system for toluene degradation by a hybrid ANN and NSGA-II method, Appl. Catal. B 244 (2019) 107–119.

[68] N. Jiang, N. Lu, K. Shang, J. Li, Y. Wu, Innovative approach for benzene degradation using hybrid surface/packed-bed discharge plasmas, Environ. Sci. Technol. 47 (2013) 9898–9903.

[69] M. Schiorlin, E. Marotta, M. Rea, C. Paradisi, Comparison of toluene removal in air at atmospheric conditions by different corona discharges, Environ. Sci. Technol. 43 (2009) 9386–9392.

[70] A.M. Vandenbroucke, R. Morent, N. De Geyter, C. Leys, Non-thermal plasmas for non-catalytic and catalytic VOC abatement, J. Hazard. Mater. 195 (2011) 30–54.

[71] H. Lee, M. Chang, Abatement of gas-phase p-xylene via dielectric barrier discharges, Plasma Chem. Plasma Process 23 (2003) 541–558.

[72] Y. Guo, D. Ye, K. Chen, J. He, W. Chen, Toluene decomposition using a wire-plate dielectric barrier discharge reactor with manganese oxide catalyst in situ, J. Mol. Catal. A Chem. 245 (2006) 93–100.

[73] X. Yao, N. Jiang, J. Li, N. Lu, K. Shang, Y. Wu, An improved corona discharge

ignited by oxide cathodes with high secondary electron emission for toluene degradation, Chem. Eng. J. 362 (2019) 339–348.

[74] W. Xu, N. Wang, Y. Chen, J. Chen, X. Xu, L. Yu, L. Chen, J. Wu, M. Fu, A. Zhu, D. Ye, In situ FT-IR study and evaluation of toluene abatement in different plasma catalytic systems over metal oxides loaded γ-Al$_2$O$_3$, Catal. Commun. 84 (2016) 61–66.

[75] H. Huang, W. Li, Destruction of toluene by ozone-enhanced photocatalysis: performance and mechanism, Appl. Catal. B 102 (2011) 449–453.

[76] V. Wagner, M.E. Jenkin, S.M. Saunders, J.C. Young, M. Pilling, Modelling of the photooxidation of toluene: conceptual ideas for validating detailed mechanisms, Atmos. Chem. Phys. 3 (2003) 89–106.

[77] J. Van Durme, J. Dewulf, W. Sysmans, C. Leys, H. Van Langenhove, Abatement and degradation pathways of toluene in indoor air by positive corona discharge, Chemosphere 68 (2007) 1821–1829.

[78] J. Lia, H. Na, X. Zeng, T. Zhu, Z. Liu, In situ DRIFTS investigation for the oxidation of toluene by ozone overMn/HZSM-5, Ag/HZSM-5 and Mn–Ag/HZSM-5 catalysts, Appl. Surf. Sci. 311 (2014) 690–696.